AVO NMO

Jonathan Downton and Laurence R. Lines

ABSTRACT

Traditionally, AVO is performed on NMO-corrected gathers. However, NMO correction is principally a kinematic correction that distorts the amplitude and character in an offset dependent fashion. This leads to bias and error in subsequent AVO reflectivity estimates. This paper develops a simultaneous AVO-NMO inversion methodology thereby avoiding these distortions. Since the inversion problem is ill-conditioned, frequency data and *a priori* reflectivity constraints are introduced to improve the condition number of the problem.

The methodology is demonstrated on a synthetic and real data example. The synthetic example shows that the AVO-NMO methodology introduces less bias and error into the reflectivity estimates. Further, the frequency bandwidth and signal-to-noise of the AVO-NMO synthetic results are better than the AVO estimates after NMO correction. The data example also shows that the AVO-NMO reflectivity estimates have higher frequency and better signal-to-noise ratios.

INTRODUCTION

The input to AVO inversion, such as Fatti et al. (1994), Shuey (1985), Smith and Gidlow (1987), for most land seismic is NMO-corrected CDP gathers. The convolutional model is assumed to apply after NMO correction so that the AVO inversion can be performed on a time-sample by time-sample basis. We call this the "traditional methodology". There are a number of issues with the traditional methodology that lead to bias and error in the AVO estimates.

NMO correction is a kinematic correction. It is more concerned with the positioning rather than the amplitudes of the events. Claerbout (1992) points out that NMO correction is a conjugate operation, not an inverse operation. As such it introduces amplitude and character distortions. NMO stretch is one of the most familiar forms of this. For two isolated reflectors, Dunkin and Levin (1973) describe NMO stretch analytically with the expression

$$\widetilde{S}_x(f) = \frac{1}{\alpha_x} S_x\left(\frac{f}{\alpha_x}\right), \qquad (1)$$

where S_x is the spectrum before NMO correction, $\widetilde{S}_x$ is the spectrum after NMO correction, f is frequency and α_x is the compression factor or the ratio of the time difference between the two events after and before NMO. The compression factor is always less than one, so the frequency spectrum will be shifted to lower frequencies and amplified as shown in Figure 1.

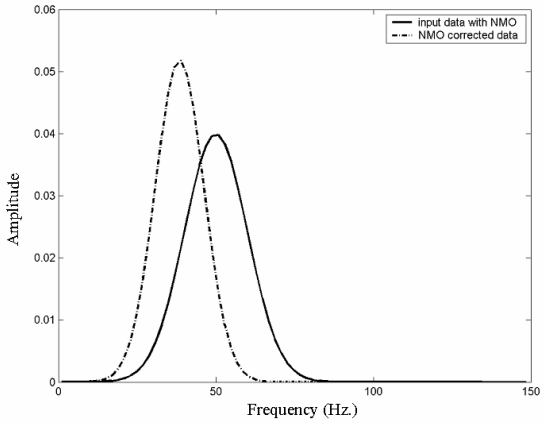

FIG. 1. Amplitude spectrum before and after NMO correction (equation 1). The NMO correction (NMO stretch) shifts the spectrum to lower frequencies and amplifies the values.

The compression factor, α_x, becomes smaller for larger offsets thus the shape of the wavelet changes in an offset dependent fashion. Figure 2, for example, shows a gather after NMO correction for incident angles from 0 to 45 degrees. The model generating this is a single reflector or spike that is convolved with a 5/10-60/70 Hz band-pass filter. For this to match the assumptions of the traditional methodology, the reflector after NMO must have constant waveform and amplitude. It does not. The far offsets are noticeably lower frequency than the near offsets and the overall character changes as a function of offset.

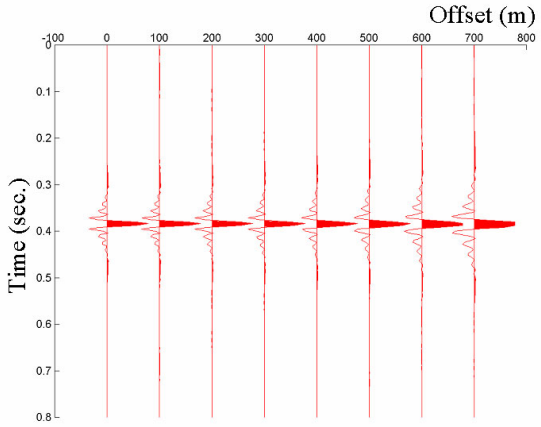

FIG. 2. Synthetic gather of a single spike after NMO and band-pass filter 10/14-60/70 Hz for incident angles from 0 to 45 degrees. Note how NMO stretch lowers the frequency on the far offsets and changes the wavelet character.

This biases the AVO inversion and introduces error. For this example, this can intuitively be understood by calculating the intercept and gradient. The intercept of the zero crossing at 0.39 seconds is zero. The gradient at this same time is positive since the wavelet broadens as a function of offset due to NMO stretch. However, if there was no NMO stretch both the intercept and gradient would be zero. Likewise, the estimates of other AVO reflectivity attributes such as the P- and S-impedance reflectivity (Fatti et al., 1994) are biased. Both cases result in scatter in the cross-plot space. This blurs anomalies and potentially obscures small anomalies in the background trend. Figures 6 and 9 shows the bias and scatter introduced by the NMO correction in cross-plot space for the synthetic example that is to be examined in this paper.

These errors become more pronounced as the maximum angle used for the AVO inversion is increased. In contrast, the uncertainty of AVO reflectivity estimates due to random noise decreases as the range of angles used for the inversion increases (Downton and Lines, 2001a) suggesting the need to trade off the two concerns. Further, three term AVO inversions, inverting for density, require gathers with large-incidence angles for accurate results. There would be an advantage if we could keep larger offsets but minimize distortions introduced in doing so.

The fact NMO stretch introduces this error raises the question why don't we use equation (1) to back out the effects of NMO stretch? Equation 1 is an approximation so we would be better off asking, "why don't we use the exact inverse for the NMO operator rather than the conjugate operator?" Unfortunately, offset-dependent tuning introduces notches into the frequency spectrum or null spaces so that the inversion in both cases is underdetermined and ill-conditioned. Conceptually, this can be understood by noting that the reflectivity of the "far-offset trace" is time delayed and squeezed into a smaller time window relative to that of the "zero-offset trace". If both the zero-offset and the far-offset reflectivity data are high-cut filtered, the far-offset data will contain less information after filtering than the near-offset data. It is the combination of the high-cut filter and the NMO operator that introduces the null space.

To address these issues, there have been a variety of methodologies proposed in the literature. Ursin and Ekren (1995) suggested flattening the CDP gather on a particular event rather that performing NMO and then performing AVO. This avoids NMO stretch, but does not deal with the offset dependent tuning. In a subsequent paper, Bakke and Ursin (1998) suggested a way to correct for offset dependent tuning. However, in deriving this, there are too many restrictive assumptions to apply in a general fashion. Swan (1997) suggests a wavelet processing approach to correct the gradient. The approach restricts one to an intercept, gradient AVO analysis and does not consider the third term. Castoro et al. (2001) suggested inverting Equation 1 to remove the NMO stretch and smoothing to deal with the null space issues.

In contrast, this paper advocates solving the NMO and AVO inverse problems simultaneously. By setting up the problem this way, the offset-dependent tuning is built into the model and NMO stretch is not an issue since it is never performed. This approach models the earth more precisely than the preceding literature. The problem is ill-posed,

but constraints similar to Downton and Lines (2001b) can be incorporated through a Bayesian framework to stabilize the problem. This paper argues that by doing AVO and NMO inversions simultaneously, better estimates of the AVO reflectivity attributes are achieved, leading to more correct trends and tighter clusters in the cross-plot domain. This is true even for events showing significant offset-dependent tuning.

In the first section of this paper, the theory of this simultaneous AVO-NMO inversion is developed. First, the convolutional AVO-NMO model is introduced, then Bayes theorem is used to incorporate constraints derived from rock physics relationships and local well-control, and finally a nonlinear optimization algorithm and uncertainty analysis is developed. The methodology is demonstrated on synthetic and real data examples. The synthetic example demonstrates that the new methodology avoids the bias and error that are present following the traditional methodology. The approach is then demonstrated on seismic data from British Columbia, Canada. The new methodology, with the addition of constraints, inverts for a higher-frequency S-impedance reflectivity with better signal-to-noise characteristics and more consistent character than the traditional methodology.

THEORY

Convolutional model

The convolutional model is used as the basis for this AVO-NMO inversion scheme. This model assumes the earth is composed of a series of flat, homogenous, isotropic layers. Plane waves are assumed, so a linear approximation to the Zoeppritz equations may be used to model how the reflectivity changes as a function of offset. Ray tracing is done to map the relationship between the angle of incidence and offset. Transmission losses, converted waves, and multiples are not incorporated in this model and so must be addressed through prior processing. In theory, gain corrections such as spherical divergence, absorption, directivity, and array corrections can be incorporated into this model, but are not considered in this paper for brevity and simplicity.

Any linear approximation of the Zoeppritz equations may be used as the starting point for this derivation including a three-term model. However, for simplicity, this paper will use the two-term Fatti approximation (Fatti et al. 1994, equation 4):

$$x(\theta) = \left(1 + \tan^2\theta\right)R_p - \left[8\left(\frac{V_s}{V_p}\right)^2 \sin^2\theta\right]R_s, \qquad (2)$$

where θ is the average angle of incidence across the interface, $x(\theta)$ is the offset dependent reflectivity, V_P and V_s are the P- and S-wave average velocity across the interface, R_P and R_S are the P- and S-impedance reflectivity respectively. If it is assumed that the background V_P/V_s ratio and relationship between angle of incidence and offset is known, then equation (2) may be written in matrix form. For example, consider the case when there are two offsets, a near-offset x_1 and a far-offset x_2, then

$$\begin{bmatrix} x_1 \\ x_2 \end{bmatrix} = \begin{bmatrix} f_1 & g_1 \\ f_2 & g_2 \end{bmatrix} \begin{bmatrix} R_P \\ R_S \end{bmatrix}, \tag{3}$$

where $f_n = 1 + \tan^2\theta,\ g_n = 8V_S^2/V_P^2 \sin^2\theta$ and the subscript indicates the offset.

Typically equation (2) is solved on an interface-by-interface basis, where each interface corresponds to a time sample. This ignores the band-limited nature of the seismic data. To address this, equation (3) can be modified to solve for multiple time samples simultaneously. To illustrate this, consider the case with two interfaces: equation (3) becomes

$$\begin{bmatrix} x_1^{(1)} \\ x_2^{(1)} \\ x_1^{(2)} \\ x_2^{(2)} \end{bmatrix} = \begin{bmatrix} f_1^{(1)} & g_1^{(1)} & 0 & 0 \\ f_2^{(1)} & g_2^{(1)} & 0 & 0 \\ 0 & 0 & f_1^{(2)} & g_1^{(2)} \\ 0 & 0 & f_2^{(2)} & g_2^{(2)} \end{bmatrix} \begin{bmatrix} R_P^{(1)} \\ R_S^{(1)} \\ R_P^{(2)} \\ R_S^{(2)} \end{bmatrix}, \tag{4}$$

where the superscript has been introduced to notate the interface number. Rearranging equation (4) so that the vectors are ordered along common offsets rather than common time samples results in

$$\begin{bmatrix} x_1^{(1)} \\ x_1^{(2)} \\ x_2^{(1)} \\ x_2^{(2)} \end{bmatrix} = \begin{bmatrix} f_1^{(1)} & 0 & g_1^{(1)} & 0 \\ 0 & f_1^{(2)} & 0 & g_1^{(2)} \\ f_2^{(1)} & 0 & g_2^{(1)} & 0 \\ 0 & f_2^{(2)} & 0 & g_2^{(2)} \end{bmatrix} \begin{bmatrix} R_P^{(1)} \\ R_P^{(2)} \\ R_S^{(1)} \\ R_S^{(2)} \end{bmatrix}, \tag{5}$$

which is further simplified by writing equation (4) as the partitioned matrix

$$\begin{bmatrix} \mathbf{x}_1 \\ \mathbf{x}_2 \end{bmatrix} = \begin{bmatrix} \mathbf{F}_1 & \mathbf{G}_1 \\ \mathbf{F}_2 & \mathbf{G}_2 \end{bmatrix} \begin{bmatrix} \mathbf{r}_P \\ \mathbf{r}_S \end{bmatrix}. \tag{6}$$

In equation (6) the vector $\mathbf{x}_n$ is the data for offset n, $\mathbf{r}_p$ and $\mathbf{r}_s$ are the P- and S-impedance reflectivity vectors, and the block matrices $\mathbf{F_n}$ and $\mathbf{G_n}$ are diagonal matrices.

AVO NMO

NMO can be written as a linear operator (Claerbout, 1992). A reflectivity sequence referenced to zero-offset time $\mathbf{x_n}$ can be transformed to offset-dependent traveltime $\mathbf{d_n}$ by the linear operator $\mathbf{N_n}$ so that

$$\mathbf{d_n} = \mathbf{N_n x_n} \tag{7}$$

The matrix $\mathbf{N_n}$ can be constructed using whatever offset traveltime relationship one desires. In order to invert data at large angles of incidence, it is important to correctly position the event without introducing residual NMO. In this case, we use a higher order correction following Castle (1994). This has the advantage of introducing high-order terms without introducing the theoretical complications of intrinsic anisotropy.

Combining equations (6) and (7) results in the set of linear equations that may be used to solve NMO and AVO simultaneously.

$$\begin{bmatrix}\mathbf{d}_1\\ \mathbf{d}_2\end{bmatrix}=\begin{bmatrix}\mathbf{N}_1\mathbf{F}_1 & \mathbf{N}_1\mathbf{G}_1\\ \mathbf{N}_2\mathbf{F}_2 & \mathbf{N}_2\mathbf{G}_2\end{bmatrix}\begin{bmatrix}\mathbf{r}_P\\ \mathbf{r}_S\end{bmatrix}. \tag{8}$$

Equation (8) may be generalized for more offsets and interfaces. Ultimately J/2 interfaces are solved based on K observations. Note that **N**, **F,** and **G** are sparse matrices that can be quickly calculated.

Prestack Processing

After processing, the prestack seismic data is typically filtered and muted thus the model needs to incorporate these processes. It is desirable that the forward model has the same wavelet as the seismic. Once this wavelet is found, it may be applied as a matrix operator, **W,** to both the right- and left-hand sides of equation (8).

The two-term Fatti et al. (1994) approximation (equation 2) is a truncated polynomial of a linear approximation of the Zoeppritz equation. It is only valid for subcritical angles becoming less accurate as the angle of incidence approaches critical θ_c. For this reason, the data is typically inverted only over some predefined angle range from θ_L to θ_H. Thus the elements of the $\mathbf{F_n}$ and $\mathbf{G_n}$ operators are zeroed outside this prescribed angle range or for supercritical reflections, thus:

$$f_n^{(i)}=\begin{cases}\left(1+\tan^2\theta_n^{(i)}\right) & \theta_L\le\theta_n^{(i)}\le\theta_H\\ 0 & \theta_n^{(i)}<\theta_L,\theta_n^{(i)}>\theta_H,\theta_n^{(i)}\ge\theta_c\end{cases}, \tag{9}$$

$$g_n^{(i)}=\begin{cases}8\left(\frac{V_s}{V_p}\right)^2\sin^2\theta_n^{(i)} & \theta_L\le\theta_n^{(i)}\le\theta_H\\ 0 & \theta_n^{(i)}<\theta_L,\theta_n^{(i)}>\theta_H,\theta_n^{(i)}\ge\theta_c\end{cases}. \tag{10}$$

For the seismic data to match the model, it is necessary to mute the seismic in a similar fashion. Lastly, if the seismic data has been muted to suppress coherent noise, this must also be incorporated. Applying the wavelet, **W,** and mute, **M,** matrix operators in series results in:

$$\begin{bmatrix}\widetilde{\mathbf{d}}_1\\ \widetilde{\mathbf{d}}_2\end{bmatrix}=\begin{bmatrix}\mathbf{MWN}_1\mathbf{F}_1 & \mathbf{MWN}_1\mathbf{G}_1\\ \mathbf{MWN}_2\mathbf{F}_1 & \mathbf{MWN}_2\mathbf{G}_2\end{bmatrix}\begin{bmatrix}\mathbf{r}_p\\ \mathbf{r}_s\end{bmatrix}, \tag{11}$$

where seismic data, $\mathbf{d_n}$, is written with a tilda to indicate it is filtered and muted. In a similar fashion, matrix operators could be introduced to account for spherical divergence, absorption, free surface, directivity, and array corrections.

Due to the band-pass filtering applied to the prestack seismic processing prior to inversion, there exists a null space corresponding to certain frequencies in the solution. To make the problem better conditioned, frequency constraints may be introduced. For frequencies where there is no information, the solution is defined to be zero, thus making

the solution smoother in the time domain than if these frequencies where left unconstrained. The constraints are implemented by creating a modified Fourier kernel matrix operator, **U**, that transforms the solution from the time domain to the frequency domain over the frequency range that contributes no information and equates these frequencies to zero, thus **Ur=0**. With the addition of these constraints, equation (11) becomes

$$\begin{bmatrix} \widetilde{\mathbf{d}}_1 \\ \widetilde{\mathbf{d}}_2 \\ \mathbf{0} \\ \mathbf{0} \end{bmatrix} = \begin{bmatrix} \mathbf{MWN}_1\mathbf{F}_1 & \mathbf{MWN}_1\mathbf{G}_1 \\ \mathbf{MWN}_2\mathbf{F}_1 & \mathbf{MWN}_2\mathbf{G}_2 \\ \mathbf{U} & \mathbf{0} \\ \mathbf{0} & \mathbf{U} \end{bmatrix} \begin{bmatrix} \mathbf{r}_p \\ \mathbf{r}_s \end{bmatrix}. \tag{12}$$

To simplify further analysis, equation (12) is rewritten as the simple linear equation

$$\mathbf{d}=\mathbf{L}\mathbf{m}, \tag{13}$$

where the linear operator, **L,** represents the matrix operator in equation (12): **d,** the data vector in equation (12): and, **m,** the unknown parameter vectors describing the band-passed P- and S- impedance reflectivity.

Still, solving for these unknown reflectivity vectors is an ill-posed problem. To understand this, note that the AVO problem is typically overdetermined, while the NMO problem is underdetermined for the reasons outlined in the introduction. This means that linear operator in equation (13) is mixed-determined and its inverse will be ill-conditioned. To make the problem better-conditioned, constraints can be introduced using a Bayesian framework.

Bayesian Inversion

Bayes' theorem provides a theoretical framework to make probabilistic estimates of the unknown parameters **m** from uncertain data and *a priori* information. The resulting probabilistic parameter estimates are called the Posterior Probability Distribution function (PDF). The PDF, written as $P(\mathbf{m}|\mathbf{d},I)$ symbolically indicates the probability of the parameter vector, **m,** given the data vector, **d,** and information, I. Bayes' theorem,

$$P(\mathbf{m} \mid \mathbf{d}, I) = \frac{P(\mathbf{d} \mid \mathbf{m}, I)P(\mathbf{m} \mid I)}{P(\mathbf{d} \mid I)}, \tag{14}$$

calculates the PDF from the likelihood function $P(\mathbf{d}|\mathbf{m},I)$ and *a priori* probability function $P(\mathbf{m}|I)$. The denominator $P(\mathbf{d}|I)$ is a normalization function which may be ignored if only the shape of the PDF is of interest

$$P(\mathbf{m} \mid \mathbf{d}, I) \propto P(\mathbf{d} \mid \mathbf{m}, I)P(\mathbf{m} \mid I). \tag{15}$$

The most likely estimate occurs at the maximum of the PDF. The uncertainty of the parameter estimate is proportional to the width of the PDF.

If uncorrelated Gaussian noise is assumed, then the likelihood function may be written as (Sivia, 1996):

$$P(\mathbf{d} \mid \mathbf{m}, I) \propto (2\pi)^{-N/2}\left(\prod_{k=1}^{K}\sigma_k^{-1}\right)\exp\left[-\frac{\sum_{k=1}^{K}\left(\sum_{j=1}^{J}L_{kj}m_j - d_k\right)^2}{2\sigma_k{}^2}\right], \qquad (16)$$

where σ_k^2 is the variance of the noise for the k^{th} observation. For AVO inversion of a single interface, it is possible to visualize the PDF since there are only two parameters. The PDF is a bivariate Gaussian function and the equiprobable solution is an ellipse. For the general case of solving the band-passed P- and S-impedance reflectivity for multiple interfaces the PDF is a multivariate Gaussian function.

A priori constraints

One way to reduce the uncertainty is to impose constraints on the solution. For example, non-physical solutions, such as reflectivity values greater than 1, can be excluded from the solution space. This can be written in terms of a uniform probability distribution where physical solutions are equiprobable and the non-physical solutions are given zero probability.

It is not necessarily desirable to assign uniform probabilities over the range of physically valid reflectivity. The stratigraphic sequence is a result of cyclic geologic processes that should result in some reflectivity values being more probable than others. Todoeschuck et al. (1990) shows that over a window where the geology is relatively consistent, the reflectivity statistics can be modeled using a Gaussian distribution. Other probability functions may be used if more appropriate, but this paper assumes Gaussian statistics to derive its results. The joint probability distribution for the P- and S-impedance reflectivity is the bivariate Gaussian distribution,

$$P(r_p, r_s \mid I) \propto \exp\left[-\frac{1}{2}\begin{bmatrix} r_p & r_s \end{bmatrix}\mathbf{C}_\mathbf{m}^{-1}\begin{bmatrix} r_p \\ r_s \end{bmatrix}\right], \qquad (17)$$

that is parameterized by a covariance matrix

$$\mathbf{C}_\mathbf{m} = \begin{bmatrix} \sigma_{r_p}^2 & \sigma_{r_{ps}} \\ \sigma_{r_{ps}} & \sigma_{r_s}^2 \end{bmatrix}. \qquad (18)$$

The diagonal elements of this covariance matrix are the variances of the P- and S-impedance reflectivity, $\sigma_{r_p}^2$ and $\sigma_{r_s}^2$. The off-diagonal element, $\sigma_{r_{ps}}$, describes how correlated the P- and S-impedance reflectivity are.

This parameter covariance matrix can be constructed from empirical rock physics relationships. The mudrock relationship (Castagna et al., 1985) is a linear relationship,

$V_p = aV_s + b,$ linking the P- and S-velocity for mudrocks. From this, Smith and Gidlow (1986) derived the fluid stack showing that for water-saturated mudstones the P and S-velocity reflectivity, r_{Vp}, and, r_{Vs}, are related by $r_{Vp} \approx a(V_s / V_p) r_{Vs}$. In a similar fashion, Fatti et al. (1994) showed that P- and S-impedance reflectivity are related by

$$r_p \approx a(V_s / V_p) r_s . \tag{19}$$

The degree to which this relationship holds is described by the correlation coefficient, R, where

$$R = \frac{\sigma_{Rps}}{\sigma_{r_p} \sigma_{r_s}}. \tag{20}$$

Other lithologies may be modeled by linear or simple polynomial relationships linking the P- and S- velocity but with different coefficients. (Castagna et al., 1993). These coefficients should ideally be calibrated based on local well-control. If the lithology is poorly understood a linear model can still be used but the correlation coefficient will probably be much lower.

With prior knowledge of the geology and the above relationships, it is possible to calculate the covariance matrix (equation 18) and thus the *a priori* probability distribution (equation 17). If we know the lithology, hence the mudrock slope, *a*, the P-impedance reflectivity variance, $\sigma^2_{r_p}$, and having previously assumed we know the background V_p/V_s ratio, then one can predict the S-impedance reflectivity variance, $\sigma^2_{r_s}$, using equation (19). The covariance, $\sigma_{r_{ps}}$, may be calculated using equation (20) from the correlation coefficient, and the P- and S- impedance variances.

However, we are not just solving the reflectivity for one interface, we are solving it for *J*/2 interfaces and hence for *J* parameters. The joint probability distribution for the P- and S-impedance reflectivity becomes the multi-variate Gaussian distribution,

$$P(\mathbf{r_p}, \mathbf{r_s} \mid I) \propto \exp\left[-\frac{1}{2} \begin{bmatrix} \mathbf{r_p} & \mathbf{r_s} \end{bmatrix} \mathbf{C_m^{-1}} \begin{bmatrix} \mathbf{r_p} \\ \mathbf{r_s} \end{bmatrix} \right], \tag{21}$$

where the covariance matrix is now *J* by *J*. If the typical assumption made in deconvolution, that each reflection coefficient is statistically independent, is held then the covariances between reflection coefficients of different time samples are all zero. Under this assumption, the covariance matrix (equation 18) describing a single interface can be used to construct the covariance matrix,

$$C_m = \left[\begin{array}{ccc|ccc} \sigma^2_{r_{p1}} & \cdots & 0 & \sigma_{r_{ps1}} & \cdots & 0 \\ \vdots & \ddots & \vdots & \vdots & \ddots & \vdots \\ 0 & \cdots & \sigma^2_{r_{pN}} & 0 & \cdots & \sigma_{r_{psN}} \\ \hline \sigma_{r_{ps1}} & \cdots & 0 & \sigma^2_{r_{s1}} & \cdots & 0 \\ \vdots & \ddots & \vdots & \vdots & \ddots & \vdots \\ 0 & \cdots & \sigma_{r_{psN}} & 0 & \cdots & \sigma^2_{r_{sN}} \end{array}\right], \qquad (22)$$

used in equation (21). In calculating this covariance matrix, $\mathbf{C}_m$, values for the P-impedance reflectivity variance, $\sigma^2_{r_p}$, and the correlation coefficient, R, can be determined by studying local well logs.

Alternatively, depending on the availability and quality of well log information in an area, it might be simpler to calculate the covariance matrix (equation 22) directly from the sample statistics of the well logs.

Nonlinear inversion

The Likelihood function (equation 16) may be combined with the *a priori* probability function (equation 21) using Bayes' theorem equation (15). The frequency- and time-domain data constraints will have different variances, each of which is assumed to be uniform. The variance of the frequency constraint misfit can be set arbitrarily to some small number so as to force the frequency constraints to be honored. There is no explicit interest in the variance of the time-domain constraints so it is marginalized (Sivia, 1996). The most likely solution can then be found by finding where the PDF is stationary. This involves taking the partial derivatives with respect to each parameter, setting the result to zero, and solving the set of simultaneous equations. This results in the nonlinear equation

$$\mathbf{m} = \left[\mathbf{L}^{\mathrm{T}}\mathbf{L} + \frac{2\boldsymbol{\varepsilon}^T\boldsymbol{\varepsilon}}{(K-1)Q}\mathbf{C}^{-1}{}_m\right]^{-1}\mathbf{L}^T\mathbf{d}, \qquad (23)$$

where $\boldsymbol{\varepsilon}=\mathbf{Lm-d}$ and $Q = \mathbf{m}^T\mathbf{C}_m^{-1}\mathbf{m}$ **.** The equation is weakly nonlinear and can be solved in an iterative fashion using Newton-Raphson or conjugate gradient. The term $\boldsymbol{\varepsilon}^{\mathrm{T}}\boldsymbol{\varepsilon}$ is an estimate of the RMS energy of the noise, and Q, the $\mathbf{C}_m^{-1}$ norm of the signal. The ratio is therefore an estimate of the N/S ratio. The ratio acts as a weighting factor determining how much the prior constraints influence the solution. If the S/N is large, then the weighting factor is small and the constraints add little to the solution and vice versa.

Uncertainty analysis

The uncertainty of the parameter estimate is related to the width of the distribution. This can be calculated from the second derivative evaluated at the parameter estimate. Assuming uniform, uncorrelated, Gaussian noise, the parameter covariance matrix,

$$\mathbf{C}_d = \left[\mathbf{L}^{\mathrm{T}}\mathbf{L} + \frac{2\boldsymbol{\varepsilon}^T \boldsymbol{\varepsilon}}{(K-1)Q} \mathbf{C}^{-1}{}_m \right]^{-1}, \tag{24}$$

describes the uncertainty. The diagonal of the covariance matrix represents the variance of each parameter estimate. The off-diagonal element represents the degree of correlation between the errors.

RESULTS

Synthetic example

The synthetic model is based on Swan's, (1997) Table 1, shown in Figure 3. The synthetic gather (Figure 10a) was generated using the Zoeppritz equation, raytracing a 10/14-60/70 Hz wavelet with random noise introduced to give a 10-to-1 S/N ratio. The top and base of each reflector complex tunes in an offset-dependent fashion. Swan demonstrates that this tuning introduces a bias to the gradient and hence, in our case, a distortion to the S-impedance reflectivity.

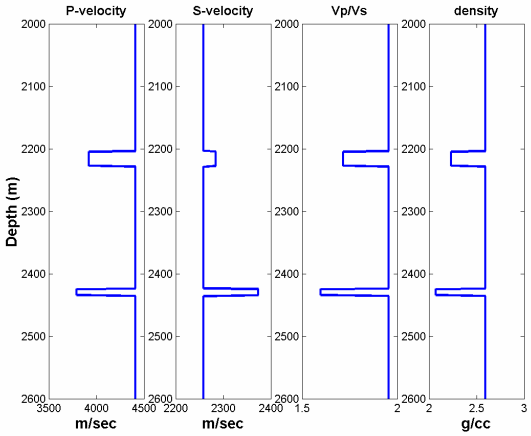

FIG. 3. Velocity and density input to synthetic model following Swan's (1997) Table 1.

Figure 4 demonstrates the distortions that are introduced by applying the traditional methodology of first applying NMO and then doing the AVO analysis.

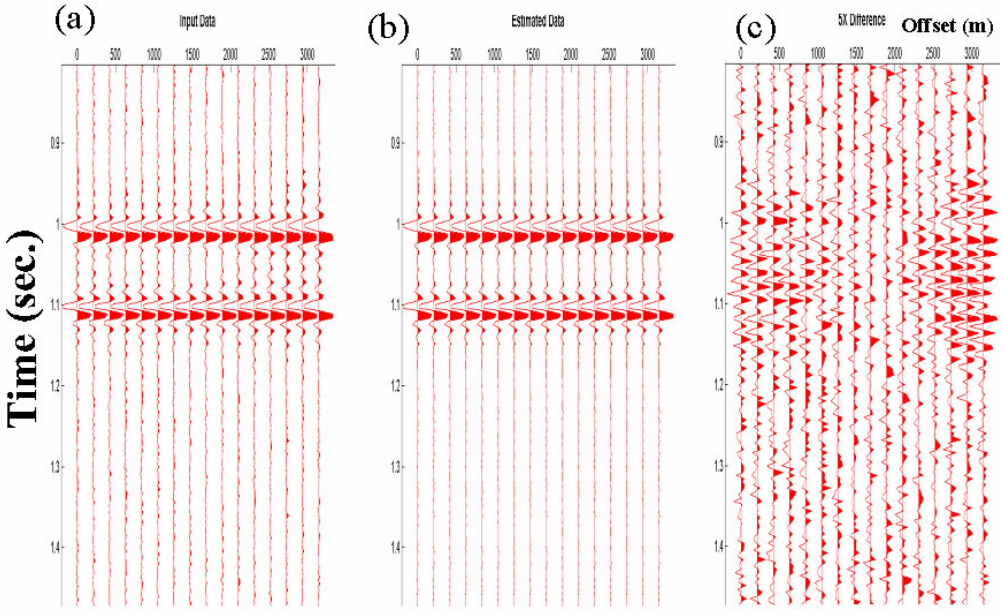

FIG. 4. The left panel (a) shows a synthetic gather generated by the Zoeppritz equation and ray-tracing followed by a 10/14-60/70 Hz band-pass filter and NMO correction. Random noise is introduced to give a 10-to-1 S/N ration. The middle panel (b) shows the estimate of the data after performing AVO inversion on NMO corrected input gathers. The right panel (c) shows 5X the difference between the input gather and estimated data. Note the high-frequency harmonic noise that has been introduced by the NMO correction.

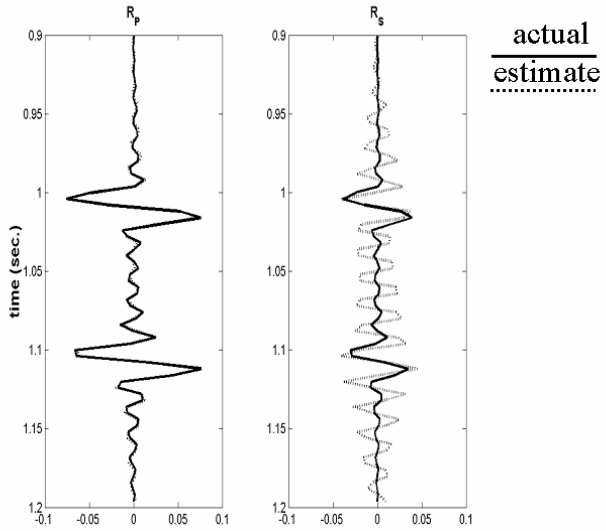

FIG. 5. The P- and S-impedance reflectivity estimated by the AVO inversion (dotted line) are compared to the reference zero-offset P- and S-impedance reflectivity (solid line). Both are shown with 10/14 – 60/70 Hz. band-limits. The harmonic noise in Figure 4c causes the estimate of the S-impedance reflectivity to be poor.

Figure 4b shows the estimated data, $\hat{\mathbf{d}}$, after estimating the P- and S-impedance reflectivity, $\hat{\mathbf{m}}$, on a sample-by-sample basis using the NMO-corrected gather (Figure 4a) as the input to the AVO inversion. The estimated data is described mathematically as $\hat{\mathbf{d}} = \mathbf{G}\hat{\mathbf{m}}$, where $\mathbf{G}$ is the linear operator describing equation (2). The difference (Figure 4c) between the input and the estimated data shows high-frequency harmonic noise. This noise adversely biases the S-impedance reflectivity estimate (Figure 5) where the noise constructively interferes with itself.

The noise is introduced by the NMO correction. As the offsets increase, more NMO stretch is introduced, lowering the dominant frequency and changing the character of the wavelet. For the time-sample by time-sample AVO inversion, this leads to biased reflectivity estimates. Further, it cannot model these character changes so theoretical noise is introduced, as observed in Figure 4b.

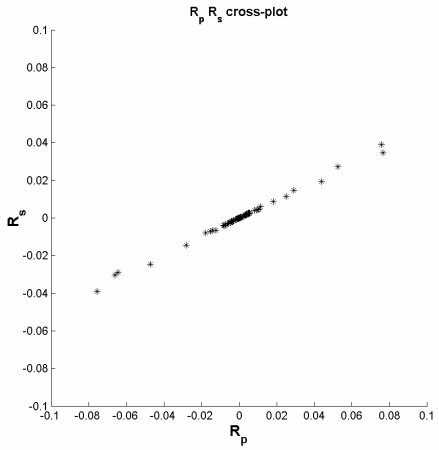

FIG. 6. Cross-plot of the results of the band-pass filtered P- and S-impedance zero-offset reflectivity (Figure 5).

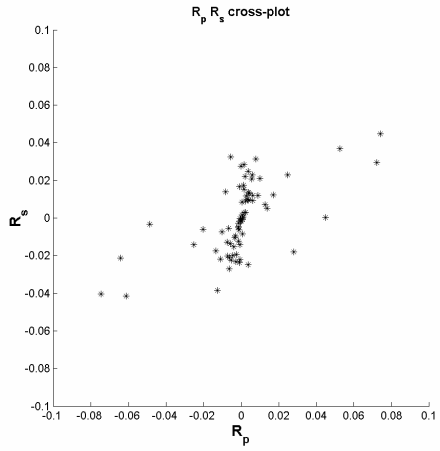

FIG. 7. Cross-plot of the results of NMO corrected AVO inversion. The input is the 10/14-60/70 Hz band-pass filtered P- and S-impedance reflectivity (Figure 5). Note that the harmonic noise introduced by the NMO correction distorts the cross-plot compared to the reference cross-plot in Figure 6. The dominant trend line has a different slope and there is much more scatter.

This noise leads to scatter and bias in the cross-plot domain. Ideally the cross-plotted P- and S- impedance reflectivity (Figure 6) should form a line whose slope is defined by the Fluid-stack relationship (equation 19). Instead the cross-plot (Figure 7) of the AVO inversion after NMO displays quite a bit of scatter and the dominant cluster has a different slope than that of the ideal case.

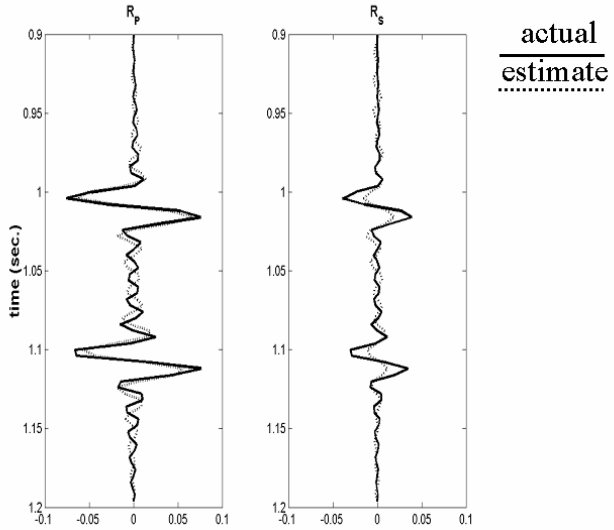

FIG. 8. The P- and S-impedance reflectivity estimated by the AVO inversion (dotted line) are compared with the reference zero-offset P- and S-impedance reflectivity (solid line). Both are shown with 10/14–50/60 Hz band-limits. By reducing the high-cut of the filter compared to Figure 5, the harmonic noise is reduced, resulting in a better S-impedance reflectivity estimate.

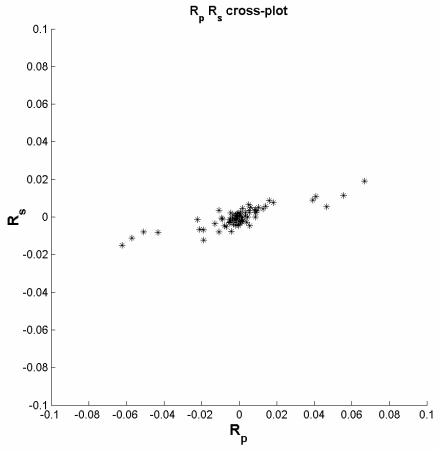

FIG. 9. Cross-plot of the results of NMO corrected AVO inversion. The input is the 10/14-50/60 Hz. band-pass filtered P- and S-impedance reflectivity (Figure 8). By reducing the high-cut filter, the scatter in the cross-plot has been reduced compared to Figure 7. However the trend line still has a different slope when compared to the reference cross-plot (Figure 6).

The effects of the NMO distortions can be abated somewhat by performing the AVO analysis at a lower frequency than what the data was modeled with. If the data is high-cut

filtered with a 50/60 Hz filter prior to the AVO analysis, the character is more consistent in an offset-dependent fashion leading to less theoretical noise. The S-impedance estimate (Figure 8) has a better character match to the ideal S-impedance though it is poorly scaled. This means that in the cross-plot domain (Figure 9), the band-passed P- and S-impedance reflectivity forms a tighter linear cluster more similar to the ideal, but with the wrong slope.

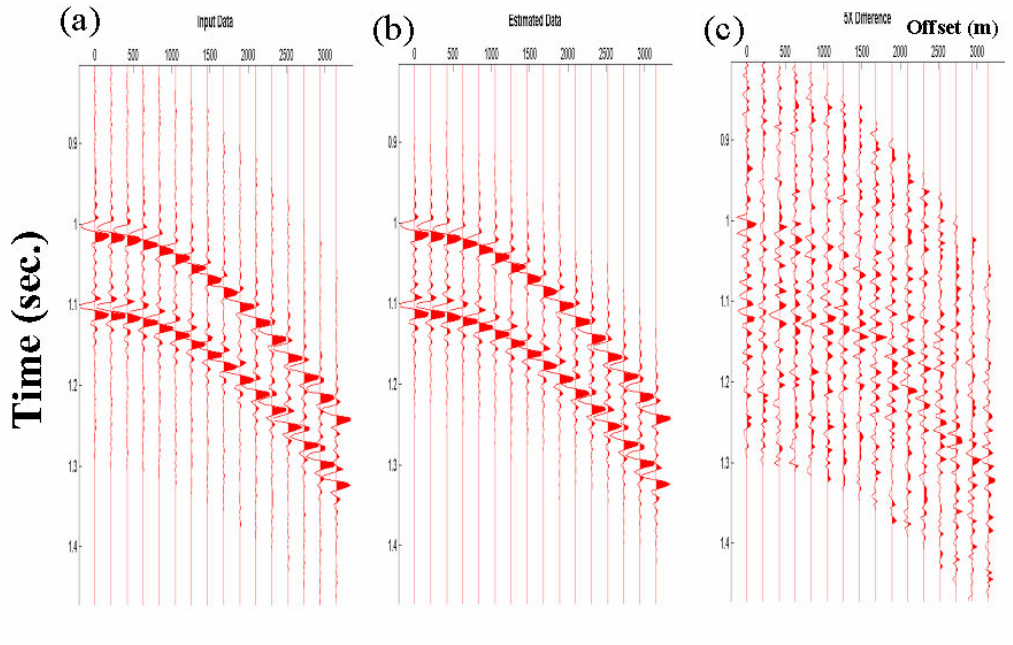

FIG. 10. The left panel (a) shows a synthetic gather generated by the Zoeppritz equation and ray-tracing followed by a 10/14-60/70 Hz band-pass filter. Random noise is introduced to give a 10-to-1 S/N ratio. The middle panel (b) shows the estimate of the data after performing AVO-NMO inversion on the input gathers. The right panel (c) shows 5X the difference between the input gather and estimated data. Note that we are no longer introducing the high-frequency harmonic noise that was evident in Figure 4.

Figures 10, 11, and 12 show the corresponding results following the methodology advocated by this paper. Figure 10 shows the difference display between the input and reconstructed model similar to Figure 4. Using the AVO-NMO methodology there is little theoretical noise introduced. The difference display (Figure 10c) mostly just identifies the random background noise that was introduced into the model. The estimated band-passed P- and S-impedance reflectivity (Figure 11) from the simultaneous AVO-NMO algorithm almost perfectly predicts the ideal reflectivity. This is confirmed by comparing the cross-plot of the estimated reflectivity (Figure 12) with the ideal (Figure 6).

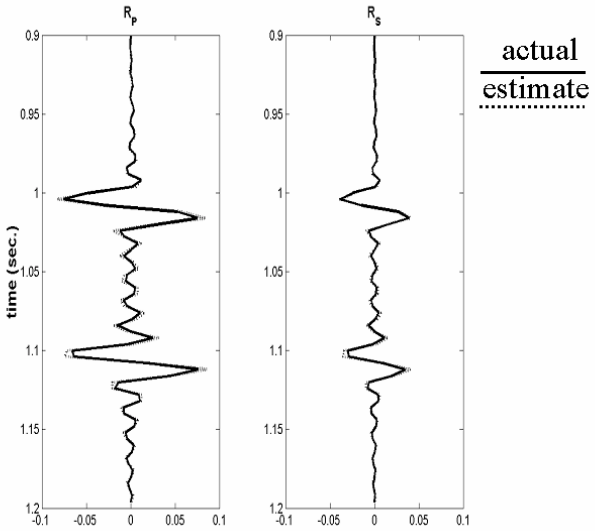

FIG. 11. The P- and S-impedance reflectivity estimated by the AVO-NMO inversion are shown with a dotted line. For reference the zero-offset P- and S-impedance reflectivity are shown with solid line. Both are shown with 10/14 – 60/70 Hz band-limits. The estimate almost is exactly the same as the reference.

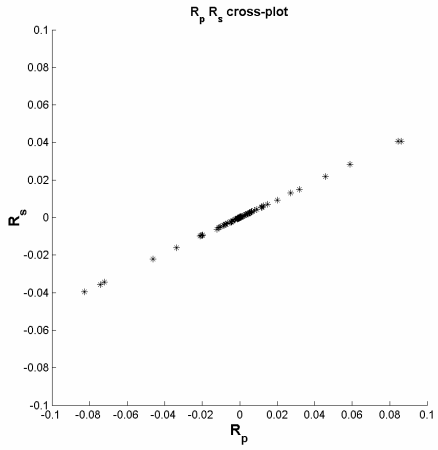

FIG. 12. Cross-plot of the results of AVO-NMO inversion. The input is the 10/14-60/70 Hz band-pass filtered P- and S-impedance reflectivity (Figure 11). The trend line and scatter are similar to the reference cross-plot (Figure 6).

Data Example

The data example is a seismic line shot to explore the Halfway sand in British Columbia, Canada. There are two bright spots on the line, one coming from a producing gas field and the other from an uneconomic gas field. The data has good signal-to-noise characteristics for incident angles up to 45 degrees. However, there is some dipping, coherent shot-related noise associated with ground conditions between CDP 1700 to 2300. The Prestack data was band-passed filtered with 10/14-110/130 Hz and had a flat frequency spectrum over the inner frequency range. By tying synthetic seismic from well-data, it was determined the seismic data was zero-phase.

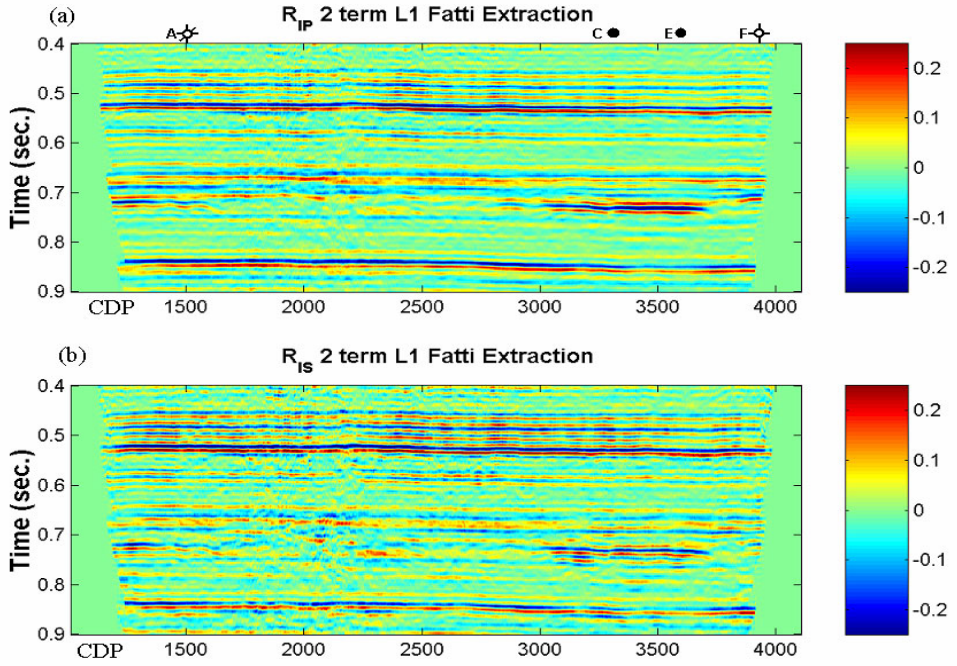

FIG. 13. Results of the traditional AVO inversion. Both the P-impedance reflectivity section (a) and the S-impedance reflectivity section (b) are shown with a 10/14-110/130 Hz filter. Note the bright spots at 0.72 seconds under the well control.

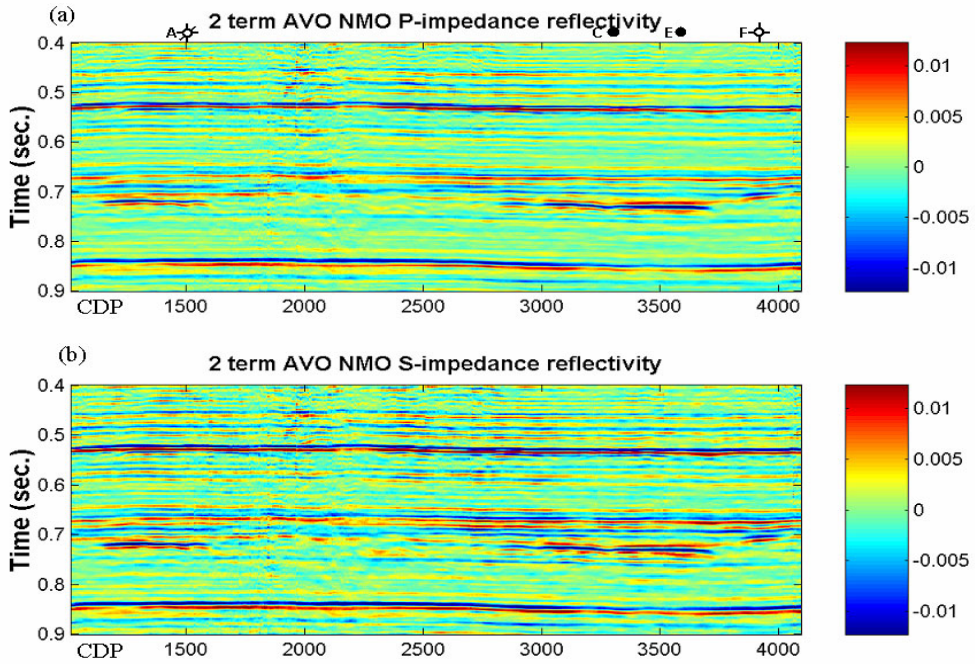

FIG. 14. Results of the AVO-NMO inversion. Both the P-impedance reflectivity section, (a), and the S-impedance reflectivity section, (b), are shown with a 10/14-110/130 Hz filter. Note the improvement in the coherency and S/N ratio of the S-impedance reflectivity inversion particularly over the interval from 0.65 to 0.75 sec. compared to the traditional AVO methodology (Figure 13). The frequency is also higher as evidenced by the clear doublet imaged at 0.68 seconds.

The data was originally processed as part of an AVO attribute study (Downton and Tonn, 1997). A robust AVO inversion using L1 statistics gave the best result at the time and is shown in Figure 13. Note the ends of the lines were muted to exclude seismic data where the maximum incidence angle was less than 17 degrees. This data was judged unreliable because of the limited range of angles available for the AVO inversion. Figure 14 shows this same line inverted using the methodology outlined in this paper. Note the increase in frequency on the S-impedance reflectivity section, particularly evident on the event at 0.67 seconds. Also, the coherency and the S/N ratio appear to be superior, particularly around the source-related noise between CDP 1700 to 2300.

DISCUSSION

These improvements come at a significant computational cost. Instead of solving N inverse problems, each with 2 parameters, the simultaneous AVO-NMO inversion solves for 2*N parameters. Solving equation (23) using Newton-Raphson involves inverting a large matrix that is time-consuming. The advantage of doing this is the calculation can also be used in the uncertainty analysis. It is possible to solve the problem more quickly, but without an uncertainty analysis, using conjugate gradient.

Two types of constraints have been introduced, the frequency-data constraints, and the *a priori* reflectivity constraints. The algorithm will work adequately with just one. The implementation of the frequency-data constraints tends to add to the diagonal of the matrix $\mathbf{L}^T\mathbf{L}$. This makes the problem better conditioned. It was found that if the range of frequencies kept were sufficiently less than the input model, then the matrix $\mathbf{L}^T\mathbf{L}$ could safely be inverted for without the *a priori* reflectivity constraints. The *a priori* reflectivity estimates were important in order to get higher frequency reflectivity estimates. The frequency data constraints, by making the problem better conditioned, reduce the uncertainty in the reflectivity estimates.

CONCLUSIONS

By inverting for both the AVO and NMO problem simultaneously using constraints, better estimates of reflectivity are obtained than if the AVO inversion is performed on NMO corrected gathers. The synthetic example showed that in cross-plot space, the AVO-NMO reflectivity estimate trends correspond more closely to the ideal, with less spurious scatter, than the traditional methodology. Further, both the synthetic and real data examples showed that the AVO-NMO reflectivity estimates have higher frequency than the traditional methodology. This is largely due to the fact that, in the traditional methodology, the data had to be restrictively filtered after NMO so as to stabilize the wavelet with offset prior to AVO inversion. This lowers the frequency content of the traditional AVO methodology reflectivity estimates. In the synthetic example, input data frequencies were recovered from the AVO-NMO reflectivity estimates.

The data example shows improvement in the coherence of events and the S/N ratio. This is due to both the constraints used to stabilize the problem. The frequency constraints add smoothness to the solution that is absent in a time-sample by time-sample inversion. The *a priori* reflectivity constraints can exclude certain non-physical or non-

probable solutions, thus de-emphasizing the influence of noise. This is evident in the superior AVO-NMO S-impedance reflectivity estimate through the portion of the data example with source-generated noise.

The parameters inverted for can be quite general. Any linear approximation of the Zoeppritz equations may be used instead of equation (2) and solved for. This basic methodology has been used to invert for three parameters including density as well.

ACKNOWLEDGEMENTS

The authors would like to thank Scott Pickford, N.S.E.R.C., and the C.R.E.W.E.S. sponsors for funding this research.

REFERENCES

Bakke, N.E. and Ursin, B., 1998, Thin-bed AVO effects: Geophys. Prosp., **46,** 571-587.

Castagna, J.P., Batzle, M.L., and Eastwood, R.L., 1985, Relationships between compressional-wave and shear-wave velocities in clastic silicate rocks: Geophysics, **50,** 571-581.

Castagna, J.P., Batzle, M.L. and Kan, T.K., 1993, Rock physics - The link between rock properties and AVO response, *in* Backus, M.M., Ed., Offset-Dependent Reflectivity - Theory and Practice of AVO Analysis: Soc. of Expl. Geophys., 135-171.

Castoro, A., White, R.E. and Thomas, R., 2001, Thin-bed AVO: Compensating for the effects of NMO on reflectivity sequences: Geophysics, **66,** 1714-1720.

Castle, R.J., 1994, Theory of normal moveout: Geophysics, **59,** 983-999.

Claerbout, J.F., 1992, Earth Soundings Analysis, Processing versus Inversion, Blackwell Scientific Publications, 110-120.

Downton, J. and Lines, L, 2001a, AVO feasibility and reliability analysis, CSEG recorder, **26**, No 6, 66-73.

Downton, J. and Lines, L., 2001b, Constrained 3 parameter AVO estimation and uncertainty analysis, 71st Ann. Mtg., Soc. Expl. Geophys., Expanded Abstracts, 251-254.

Downton, J. and Tonn, R., 1997, Reservoir quality mapping with geostatistical and neural network techniques: Presented at 1997 S.E.G. Production and Development Forum

Dunkin, J.W. and Levin, F.K., 1973, Effect of normal moveout on a seismic pulse: Geophysics, **38,** 635-642.

Fatti, J.L., Smith, G.C., Vail, P.J., Strauss, P.J., and Levitt, P.R., 1994, Detection of gas in sandstone reservoirs using AVO analysis: A 3-D seismic case history using the Geostack technique: Geophysics, **59**, 1362-1376.

Shuey, R.T., 1985, A simplification of the Zoeppritz equations: Geophysics, **50**, 609-614.

Sivia**,** D.S., 1996, Data Analysis, A Bayesian Tutorial: Oxford University Press

Smith, G.C. and Gidlow, P.M., 1987, Weighted stacking for rock property estimation and detection of gas: Geophys. Prosp., **35,** 993-1014.

Swan, H.W., 1997, Removal of offset-dependent tuning in AVO analysis, 67th Ann. Internat. Mtg: Soc. of Expl. Geophys., 175-178.

Todoeschuck, J.P., Jensen, O.G. and Labonte S., 1990, Gaussian scaling noise model of seismic reflection sequences: Evidence from well logs: Geophysics, **50**, 480-484.

Ursin, B. and Ekren, B.O., 1995, Robust AVO analysis: Geophysics, **60,** 317-326.